ADVANCED ENERGY MATERIALS
www.advenergymat.de

3D Macroporous Frame Based Microbattery With Ultrahigh Capacity, Energy Density, and Integrability

*Wei Yang, Lin Xu, Wen Luo, Ming Li, Ping Hu, Yuhang Dai, Fazhi Ye, Chunhua Han, Minxuan Zhou, Rong Tu, Ji Shi, and Liqiang Mai**

In-plane microbatteries (MBs) with features of facile integration, mass customization, and especially superior electrochemical performance are urgently required for self-powered microelectronic devices. In this work, a facile manufacturing process is employed to fabricate Zn–MnO_2 MB with a 3D macroporous microelectrode. Benefiting from the high electron/ion transport path of 3D macroporous microelectrode and high mass-loading of poly(3,4-ethylenedioxythiophene)-manganese dioxide (PEDOT-MnO_2) film, the MB achieves an ultrahigh capacity of 0.78 mAh cm^{-2} and an outstanding areal energy density of 1.02 mWh cm^{-2}. Moreover, 3D macroporous PEDOT-MnO_2 hybrid film is achieved by one-step electrodeposition, which effectively improves the cycling performance without reducing areal capacity or hindering the ion diffusion. Notably, the MB can stably drive an electronic timer for ≈400 min or be integrated and operated on the surface of a digital hygro-thermometer. The MBs are capable of operating stably in the high rotation speed and vibration condition, such as applied on the surface of an axial-flow fan. Moreover, the MB can integrate by stacking the substrate-free microelectrodes and achieving outstanding energy density of 3.87 mWh cm^{-2}. Therefore, the PEDOT-MnO_2//Zn MB has good prospects as a next-generation component applied in self-powered microelectronic devices.

1. Introduction

Miniaturized on-chip power supplies are highly required for next-generation self-powered microelectronic devices. Combining high electrochemical performance and high integration is a crucial issue for on-chip micro energy storage devices to satisfy the application in self-powered wireless microsensors, portable/implantable microelectronic devices, portable/wearable personal electronics, microelectromechanical systems, and so on.[1,2] Nowadays, micro-supercapacitors (MSCs) with interdigital electrodes have attracted wide attention from researchers due to their facile fabrication, eco-friendliness, high areal power density, and long lifespan.[3,4] However, a flat discharge plateau and high energy density are essential for many microelectronic elements that demonstrate the critical status of micro-sized batteries. As commercial on-chip micro power supplies, Li-ion film batteries with high areal energy densities and excellent integration performance have been widely applied. Still, their limited lifespan, low power density, environmental/health risk, and economic cost limit their further application for next-generation self-powered micro-electronic systems.[1] Therefore, aqueous microbatteries (MBs), compatible with high safety, superior energy/power density, nontoxicity, and simple processing, can realize the application of micro-energy storage devices (MESDs) in microelectronic devices.

To obtain interdigital microelectrodes for MESDs, active materials should be constructed in the limited patterned space by various methods, such as vacuum filtration,[5] inkjet printing,[6] photoresist carbonization,[7] and bottom–up electrodeposition.[8] The high areal energy density is crucial and is typically achieved by high areal mass-loading of active materials. Still, the rate performance significantly decays with the increase of the electron/ion transport path.[9] For microelectrodes, compared with stacking active materials on the planar surface, 3D microelectrodes with thick and internal microporous microstructure have enormous potential to increase surface area and loading of active materials per-unit footprint area. Furthermore, 3D microelectrodes are capable of offering sufficient electrolyte diffusion paths and accelerating the electron/ion transportation process, which effectively enhances the energy/power performance of the MESDs.[10] Presently, 3D microelectrodes have been widely applied in MESDs fabrication and constructed into various morphologies

W. Yang, L. Xu, W. Luo, M. Li, P. Hu, Y. Dai, F. Ye, C. Han, M. Zhou, R. Tu, L. Mai
State Key Laboratory of Advanced Technology for Materials Synthesis and Processing
School of Materials Science and Engineering
Wuhan University of Technology
Wuhan 430070, China
E-mail: mlq518@whut.edu.cn
L. Xu, P. Hu, L. Mai
Hubei Longzhong Laboratory
Wuhan University of Technology (Xiangyang Demonstration Zone)
Xiangyang 441000, China
J. Shi
School of Materials and Chemical Technology
Tokyo Institute of Technology
Tokyo 152-8552, Japan

The ORCID identification number(s) for the author(s) of this article can be found under https://doi.org/10.1002/aenm.202300574

DOI: 10.1002/aenm.202300574

such as pillar structure,[11] layer-by-layer structure,[12] vertical alignment structure,[13] interwoven nanowire structure,[14] and porous structure.[15] Among them, microelectrode with a macroporous structure is capable of offering a large surface area for active materials growth, a 3D frame for electron transport, and sufficient interspace for ion transport. Therefore, the hard template method with polystyrene opal self-assembled film was widely employed in constructing ordered 3D macroporous microelectrode and achieving MBs with high energy/power performances.[15–17] However, the disadvantages, including high costs for polystyrene nano/micro sphere, the relatively time-consuming vertical deposition process, the strict temperature and time control for post-baking, and the highly smooth requirement for electrode surface, have vastly hindered the large-scale commercial application for this method. Hence, a rapid, scalable, and low-cost manufacturing should be preferentially considered for future industrial applications. As one of the soft template methods, the hydrogen bubble template is capable of constructing a macroporous frame at a breakneck speed, has been widely adopted in the different-scale electrodes' manufacture, and achieves a 3D macroporous structure with high thickness and surface area, which realizes high capacity materials loading and achieves superior electrochemical performance.[18] Therefore, the hydrogen bubble template method has a superior advantage in microelectrode fabrication and a high potential applied in industrial MESDs manufacturing.

Among the various cathode materials for aqueous energy storage devices, Mn-based materials have a high capacity, low price, high level of safety, various commonly available valence states with relatively high electrochemical potentials (Mn^{2+}, Mn^{3+}, and Mn^{4+}), facilely achieved through electrochemical preparations.[19,20] Therefore, various Mn-based materials have been applied in energy storage, such as biphase Co–Mn–O,[21] β-MnO_2/birnessite core/shell nanostructure,[22] rod-like $Na_{0.95}MnO_2$,[23] ultralong MnO_2 nanowires,[24] and ultrathin δ-MnO_2 nanosheet.[25] In these works, Mn-based materials exhibit rich morphologies and achieve superior electrochemical performance when employed as cathodes for batteries or supercapacitors. Thus, Mn-based materials have been widely adopted as cathode electrodes for MESDs. In general, the energy density (E) depends on the capacity (C) and voltage platform (V). Hence, adopting suitable active materials and lifting voltage platforms are critical for improving energy density. As an excellent aqueous anode material, zinc has a low potential of −0.763 V (vs standard hydrogen electrode), a high capacity density of 5855 mAh cm^{-3}, safety/nontoxicity, and low cost.[26] Therefore, it has been widely established as a candidate for aqueous batteries, such as CC–CF@ZnO//CC–CF@NiO alkaline battery,[27] PPy//Zn battery,[28] and porous carbon//Zn Br–Zn static battery.[29] Recent years have witnessed the thriving development of Zn–MnO_2 aqueous MBs due to their relatively high output voltage, high capacity, facile fabrication, good safety, low-temperature application, and eco-friendliness.[30,31] Nevertheless, the present planarization design and direct active materials loading of MESDs are hard to realize high areal electrochemical performance.[32] Therefore, the breakthrough in combining 3D frame microelectrode with Zn–MnO_2 MBs to achieve high areal energy density is urgent.

2. Results and Discussion

In this work, the interdigital microelectrode was achieved by constructing a rational mass-loading poly(3,4-ethylenedioxythiophene)-manganese dioxide (PEDOT-MnO_2) film on a 3D macroporous Ni frame and further formulated to fabricate quasi-solid-state PEDOT-MnO_2//Zn MBs. The 3D macroporous Ni frame microelectrode with high thickness has a large surface area for active materials growth and provides an abundant pathway for electron/ion transport. The PEDOT-MnO_2//Zn MB has a high capacity of 0.78 mAh cm^{-2} (at 0.5 mA cm^{-2}), an ultrahigh energy density of 1.02 mWh cm^{-2} (at 0.65 mW cm^{-2}), and a relatively high power density of 12.16 mW cm^{-2} (at 0.16 mWh cm^{-2}). Notably, the MB with four layers stacked microelectrodes shows outstanding integrability and expansibility, which delivers an ultrahigh areal capacity of 2.94 mAh cm^{-2} and energy density of 3.87 mWh cm^{-2}. This MB exhibits excellent electrochemical performance, facile fabrication, and high integrability that has great potential applications in microelectronic systems.

The fabrication process of PEDOT-MnO_2//Zn is exhibited in **Figure 1**. The PEDOT-MnO_2 macroporous microelectrode is achieved through an electrodeposition process. First, Ni microelectrodes, fabricated by commercial large-scale wet etching (Figure S1a, Supporting Information), are prepared and constructed with 3D macroporous Ni microstructure on the surface by a hydrogen bubble template method (Figure 1a). Then, an electrodeposition electrolyte solution containing manganese acetate and EDOT is prepared, in which a cyclic voltammetry (CV) electrodeposition process with different cycles of 10, 30, 50, 70, and 90 is employed, and constructs a continuous thickness of PEDOT-MnO_2 film on the 3D macroporous Ni frame microelectrode (denoted as PEDOT-MnO_2-10, 30, 50, 70, and 90, respectively) (Figure 1b). In this strategy, a rational mass-loading film is capable of providing a high areal capacity relative to a low mass-loading film and combining a suitable ionic diffusion path. Still, an excessive mass-loading film will observably impede ion diffusion in the active material (Figure 1c). After that, a Zn@carbon nanotubes (CNTs) and a PEDOT-MnO_2-70 interdigital microelectrode are assembled on a polyethylene terephthalate (PET) substrate by assembly tool (Figure S1c, Supporting Information). After gel-electrolyte coating, the microelectrodes are packaged with a square polyethylene (PE) film, and the PEDOT-MnO_2//Zn MB is achieved (Figure 1d).

Figure 2a,b exhibits the scanning electron microscopy (SEM) morphology of 3D macroporous Ni microelectrode. The macroporous are uniformly distributed on the surface of one finger of the microelectrode, and the digital image of this interdigital microelectrode with four fingers exhibits fine appearance (Figure 2a inset). The macroporous are surrounded by micro Ni clusters (Figure 2b) with a high surface area, and the Ni clusters are constructed by Ni nanoparticles below 200 nm (Figure S2a, Supporting Information). Figure 2c exhibits the morphology of PEDOT-MnO_2-70 microelectrode. The surface of Ni clusters is evenly coated with PEDOT-MnO_2 composite, and the macroporous structure is well retained. Furthermore, the digital image of PEDOT-MnO_2-70 microelectrode exhibits a similar appearance to the 3D macroporous Ni frame microelectrode

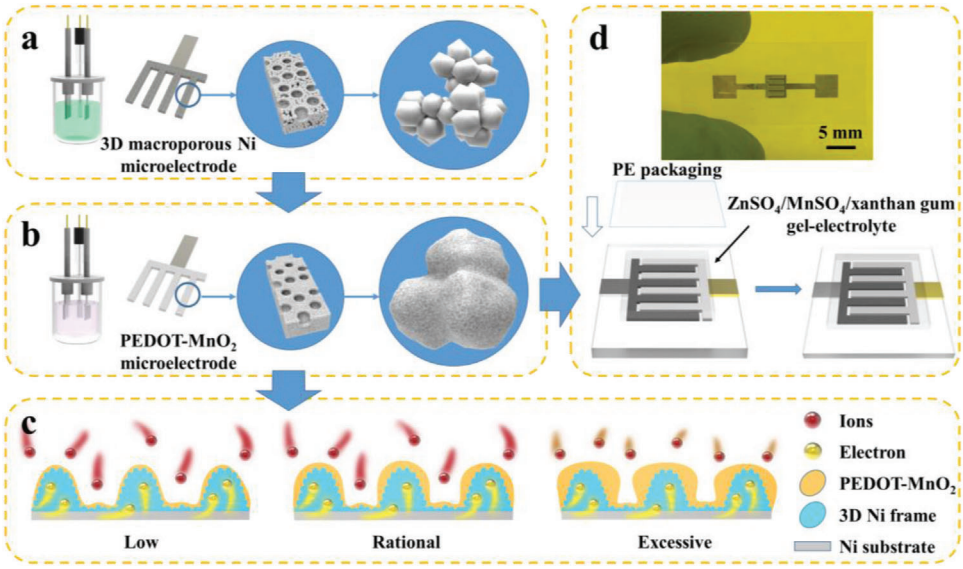

Figure 1. Schematic illustration of the fabrication processes of a) 3D macroporous Ni microelectrodes and b) PEDOT-MnO_2 microelectrodes. c) The schematic diagram for electron/ions transport in different thicknesses of PEDOT-MnO_2 film. d) Digital image for PEDOT-MnO_2//Zn microelectrodes and manufacture for quasi-solid-state PEDOT-MnO_2//Zn MB.

(Figure 2c inset), demonstrating the outstanding feasibility of this electrodeposition strategy. Compared to the chapped bulk structure of PEDOT-MnO_2-70 film on the planar microelectrode (Figure S3, Supporting Information), the 3D Ni frame is capable of offering sufficient interspace and surface area for active materials growth, the rational mass loading of PEDOT-MnO_2-70 film is capable of providing superior areal capacity, and the porous structures provide transport paths for electrolyte ions. The SEM images of PEDOT-MnO_2-10 to 90 are further collected. Compared to 3D macroporous Ni frame microelectrode, the morphology of PEDOT-MnO_2-10 appears unchanged at low magnification images. At high magnification, the Ni clusters are densely covered with nanosized PEDOT-MnO_2 composite material, and the Ni nanoparticles remain well (Figure S4, Supporting Information). With the increase of mass loading, the macroporous is covered with gradually thickened PEDOT-MnO_2 film. The macroporous structure remains well for PEDOT-MnO_2-30 and 50 (Figures S5 and S6, Supporting Information). The excessive mass-loading film appears for PEDOT-MnO_2-90 with macroporous size shrinking dramatically (Figure S8, Supporting Information), indicating the feature of continuous mass loading increase with the electrodeposition process for the strategy. Furthermore, energy dispersive spectroscopy (EDS) mapping images of the edge side of PEDOT-MnO_2-70 are exhibited in Figure 2d and verify the homogeneous distribution of Mn, S, and Ni elements, indicating the MnO_2 and PEDOT are uniform coated

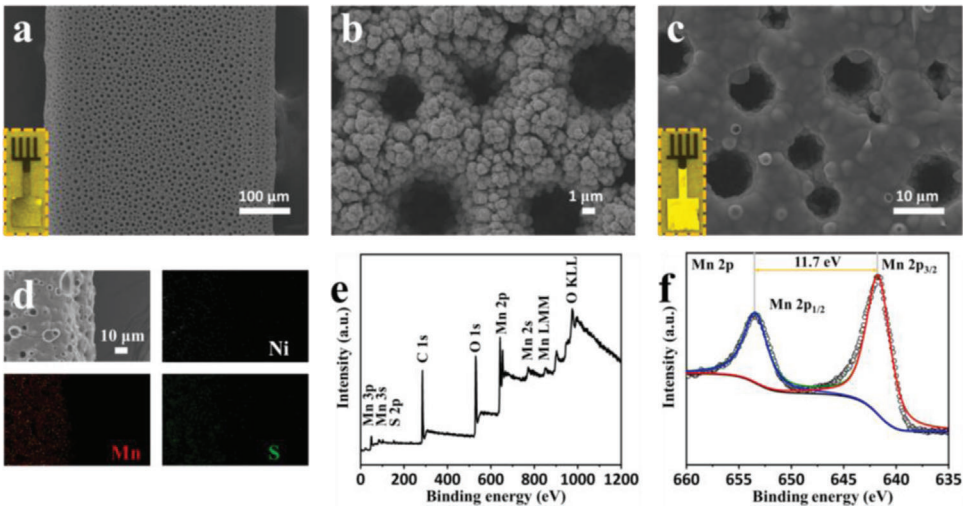

Figure 2. Structural characterizations of PEDOT-MnO_2 microelectrode. SEM images of a,b) 3D macroporous Ni frame microelectrode and c) PEDOT-MnO_2-70 microelectrode. d) EDS mapping images of Ni, Mn, and S elements. e) Full XPS spectrum and f) Mn 2p spectrum of PEDOT-MnO_2 microelectrode.

on the microelectrode. The atomic ratio of Mn and S elements of PEDOT-MnO_2-70 microelectrode is also characterized by EDS and present in Figure S9, Supporting Information. For PEDOT-MnO_2-10, 30, 50, and 90 microelectrodes, similar EDS results are also obtained, indicating the uniformity of active material deposition during this process (Figures S10–13, Supporting Information). The X-ray diffraction (XRD) patterns of Ni, porous Ni, and PEDOT-MnO_2-70 microelectrodes are exhibited in Figure S14, Supporting Information, porous Ni has high stability during the deposition process, and the electrodeposition of MnO_2 shows a low crystallinity. The Raman spectra of MnO_2-70, PEDOT-MnO_2-70, and PEDOT-70 microelectrodes are exhibited in Figure S15, Supporting Information. The obvious Raman peaks of Mn–O for MnO_2 and C=C for PEDOT can be detected in PEDOT-MnO_2-70.[20,33] The high-resolution transmission electron microscopy (HRTEM) and selected area electron diffraction (SAED) images of PEDOT-MnO_2-70 are shown in Figure S16, Supporting Information; the interplanar distance of 0.24 nm corresponds to the (100) MnO_2 (JCPDS# 30–0820) and the SAED pattern shows similar results. The PEDOT-MnO_2-70 is further characterized by X-ray photoelectron spectroscopy (XPS). As shown in Figure 2e, the XPS survey spectrum exhibits the presence of S, C, O, and Mn elements in the PEDOT-MnO_2-70 film. Figure 2f exhibits the XPS peaks of Mn $2p_{3/2}$ at 641.7 eV, and Mn $2p_{1/2}$ at 653.4 eV; the spin-energy separation of 11.7 eV corresponds to the Mn^{4+} 2p electrons.[34,35] Figure S17a, Supporting Information presents the XPS of S 2p, the binding energy for S $2p_{3/2}$ and S $2p_{1/2}$ are located at 163.3 and 164.6 eV, and a binding energy difference of 1.3 eV. The third peak, at 168.1 eV, corresponds to partially oxidized S ($S^{\delta+}$).[36,37] The O 1s peak has four obvious components, representing the peak at 529.5 eV for the Mn–O component, the peak at 530.9 eV for the C–O–C component in PEDOT, the peak at 532 eV for the Mn–O–H component, and the peak at 533.4 eV for absorbed water (Figure S17b, Supporting Information).[38]

To evaluate the electrochemical properties, a two-electrode cell is assembled. The PEDOT-MnO_2 microelectrodes are employed as cathodes, and a commercial Zn foil is employed as the anode in the aqueous electrolyte containing 2 M $ZnSO_4$ and 0.4 M $MnSO_4$. **Figure 3**a presents the discharge voltage profiles of PEDOT-MnO_2-10, 30, 50, 70, and 90 at a current density of 1 mA cm^{-2}. With the thickness of PEDOT-MnO_2 film increasing, all the curves have a prolonged discharge voltage platform situated at ≈1.2–1.4 V, and the areal capacities increase successively, indicating the 3D macroporous Ni frame offers a sufficient interspace and surface area for constructing active materials with gradually expanded mass loading. The areal specific capacities of PEDOT-MnO_2-10, 30, 50, 70, and 90 at different current densities are shown in Figure 3b. At a low current density of 1 mA cm^{-2}, the areal specific capacities of the above microelectrodes are 0.34, 0.81, 1.10, 1.42, and 1.59 mAh cm^{-2}, respectively (gravimetric capacity based on the mass of active materials is exhibited in Figure S18, Supporting Information). When the current density increases to 10 mA cm^{-2}, the capacities of PEDOT-MnO_2-10 to 70 are maintained at 0.14, 0.31, 0.41, and 0.51 mAh cm^{-2}, respectively. For PEDOT-MnO_2-90, the capacity retention notably decreases to 0.44 mAh cm^{-2} because the excessively thick film seriously hinders the diffusion of the ions and results in a poor rate performance. Therefore, compared with the above microelectrodes, the thickness of PEDOT-MnO_2-70 film is capable of achieving high mass-loading and relatively high ions diffusion simultaneously. The electrochemical impedance spectrum (EIS) is further carried out to explore the electrochemical behavior of PEDOT-MnO_2-10 to 90 microelectrodes (Figure S23, Supporting Information). The typical Nyquist plots of PEDOT-MnO_2-10 to 90 can consist of a series resistance (R_s), an interfacial resistance (R_i), and a charge transfer resistance (R_{ct}).[39] The R_s of PEDOT-MnO_2-10 to 90 microelectrodes is approximate. When the deposited film rises from PEDOT-MnO_2-10 to 90, the R_i and R_{ct} gradually increase. Moreover, the slopes of fit lines of PEDOT-MnO_2-30 to 90 gradually decrease at low-frequency, indicating their transfer/diffusion kinetics decrease gradually.[40] The galvanostatic charge/discharge (GCD) curves of PEDOT-MnO_2-70 from 1 to 10 mA cm^{-2} with a potential window of 0.9 to 1.8 V are shown in Figure 3c. With the current density increases, the charge/discharge curves exhibit stable voltage and relatively high Coulombic efficiency. In addition, the IR drop is calculated from GCD results of 7.4, 13, 18.6, 24.5, 22.9, 35.1, 40.4, 45.9, 51.7, and 56.5 mV at a current density from 1 to 10 mA cm^{-2}, respectively. The low IR drop for PEDOT-MnO_2-70 microelectrode demonstrates the 3D macroporous Ni frame, and PEDOT offers a fast electron transfer path. The high areal capacity of PEDOT-MnO_2-70 is contributed by the Mn^{2+} additive and the inserting/extracting of Zn^{2+}/H^+ (Figure S19a, Supporting Information).[41] Besides, PEDOT-MnO_2-70 and MnO_2-70 exhibit similar discharge plateau and areal capacity, indicating the low contribution of PEDOT in the charge/discharge process (Figure S19b, Supporting Information). Meanwhile, MnO_2-70 shows a poor cycling performance without PEDOT protection (Figure S19c, Supporting Information), which is consistent with previous reports.[30,42,43] The approximate GCD performances of PEDOT-MnO_2-10, 30, 50, and 90 with high Coulombic efficiency and stable discharge plateau are exhibited in Figure S22, Supporting Information, indicating the high electrochemical reliability for the PEDOT-MnO_2 films with thickness increasing. The CV curves of PEDOT-MnO_2-70 from 1 to 5 mV s^{-1} are shown in Figure 3d with a voltage from 0.9 to 1.9 V. Upon cathodic scanning of 1 mV s^{-1}, the two reduction peaks at 1.4 and 1.2 V peak correspond to Mn^{4+} reduction to Mn^{3+}, which approximate to the GCD results. To study the charge storage mechanism of the PEDOT-MnO_2-70 microelectrode, Dunn's method is employed to separate the current contributions of capacitive contribution (shaded region) and diffusion-controlled contribution (blank region) (Figure 3e; Figure S24, Supporting Information).[44] The diffusion-controlled and capacitive contributions to the total stored charge of the PEDOT-MnO_2-70 microelectrode at different scan rates are shown in Figure 3f. With the scan rates rising from 1, 2, 3, and 4 to 5 mV s^{-1}, the ratios of contribution determined by the capacitive process increase steadily from 51.4%, 66.2%, 72.7%, and 76.5%, to 85.4%, respectively. To determine the reaction kinetic of PEDOT-MnO_2-70 and MnO_2-70, the galvanostatic intermittent titration technique (GITT) is employed. Figure 3g–i illustrates the GITT curves and the ions diffusion coefficients of PEDOT-MnO_2-70 and MnO_2-70 microelectrodes. The two obvious discharge plateaus correspond to the diffusion coefficient values, indicating the fast H^+ insertion of plateaus I and slow Zn^{2+} insertion of plateaus II, respectively.[45,46] Moreover, the similar GITT curves and corresponding ion

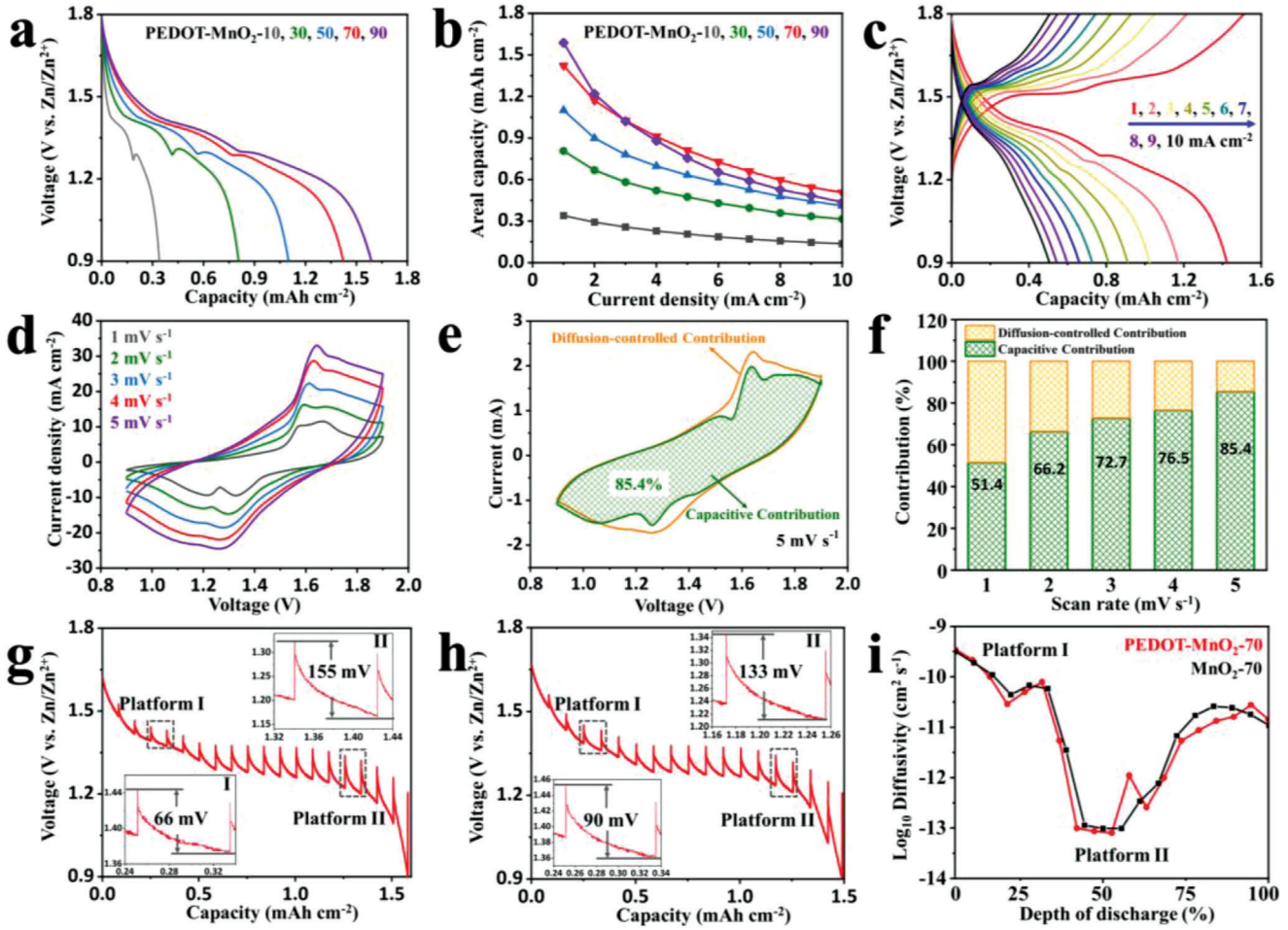

Figure 3. Electrochemical performance of PEDOT-MnO_2-10, 30, 50, 70, and 90 microelectrodes. a) Discharge curves at a current density of 1 mA cm^{-2} and b) areal capacities at various current densities. c) GCD curves of PEDOT-MnO_2-70 at various current densities. d) CV curves of PEDOT-MnO_2-70 at different scan rates and e) from 0.9 to 2.1 V with shadowed area exhibiting the capacitive contribution. f) Separations of capacitive and diffusion-controlled contribution at different scan rates for PEDOT-MnO_2-70 microelectrode. GITT curves during the discharge and charge process for g) PEDOT-MnO_2-70 and h) MnO_2-70 microelectrodes. i) Ionic diffusion coefficient derived from GITT curves during the discharge and charge process for PEDOT-MnO_2-70 and MnO_2-70 microelectrodes.

diffusion coefficients of PEDOT-MnO_2-70 and MnO_2-70 indicate that similar storage mechanism occurred in the two microelectrodes.

Electrochemical performances of quasi-solid-state PEDOT-MnO_2//Zn MB are shown in **Figure 4**. The CV profiles of PEDOT-MnO_2//Zn MB at varying scan rates from 1 to 5 mV s^{-1} are exhibited in Figure 4a. With the scan rates increasing, the CV curves show an analogous shape, demonstrating a superior rate performance and a highly reversible redox reaction. Figure 4b shows the GCD curves of the PEDOT-MnO_2//Zn MB at various current densities ranging from 0.5 to 10 mA cm^{-2}, exhibiting a discharge platform from 1.2 to 1.4 V, consistent with the CV results. Moreover, the PEDOT-MnO_2//Zn MB shows an ultrahigh areal capacity of 0.78 mA cm^{-2} at the current density of 0.5 mA cm^{-2} and capacity retention of 32% at the current density of 5 mA cm^{-2} (Figure S25, Supporting Information). The MB exhibits considerable capacity retention of 77% after 1000 cycles at a current density of 15 mA cm^{-2} (Figure S26, Supporting Information). The overall performance of the PEDOT-MnO_2//Zn MB was evaluated with the Ragone plot related to the areal energy density and areal power density (Figure 4c). PEDOT-MnO_2//Zn MB delivered an ultrahigh areal energy density of 1.02 mWh cm^{-2} at the power density of 0.65 mW cm^{-2}. This ultrahigh energy density exceeded most reported aqueous micro energy storage devices, about VO_2(B)-MWCNTs//Zn MB of 0.189 mWh cm^{-2},[47] carbon//Zn MSC of 0.115 mWh cm^{-2},[48] Na-MnO_2//Zn MB of 0.087 mWh cm^{-2},[49] CNT//Zn MSC of 0.03 mWh cm^{-2},[50] ITO-MnO_2 MSC of 0.027 mWh cm^{-2},[51] MnO_2@Ppy//Ppy MSC of 0.012 mWh cm^{-2},[52] and MnHCF-MnO_x MSC of 0.002 mWh cm^{-2}.[53] Moreover, PEDOT-MnO_2//Zn MB could offer a maximum power density of 12.16 mW cm^{-2}, which towered over the Ni-MnO_2//Zn MB of 0.0013 mW cm^{-2} with a similar max areal energy density.[32] Furthermore, the volumetric performance of PEDOT-MnO_2//Zn MB was calculated (Figures S27 and S28, Supporting Information), achieving a maximum volumetric energy density of 56 mWh cm^{-3}. To demonstrate the electrochemical performance of active materials, we ignored the thickness of the Ni interdigital microelectrode of 100 μm and achieved a

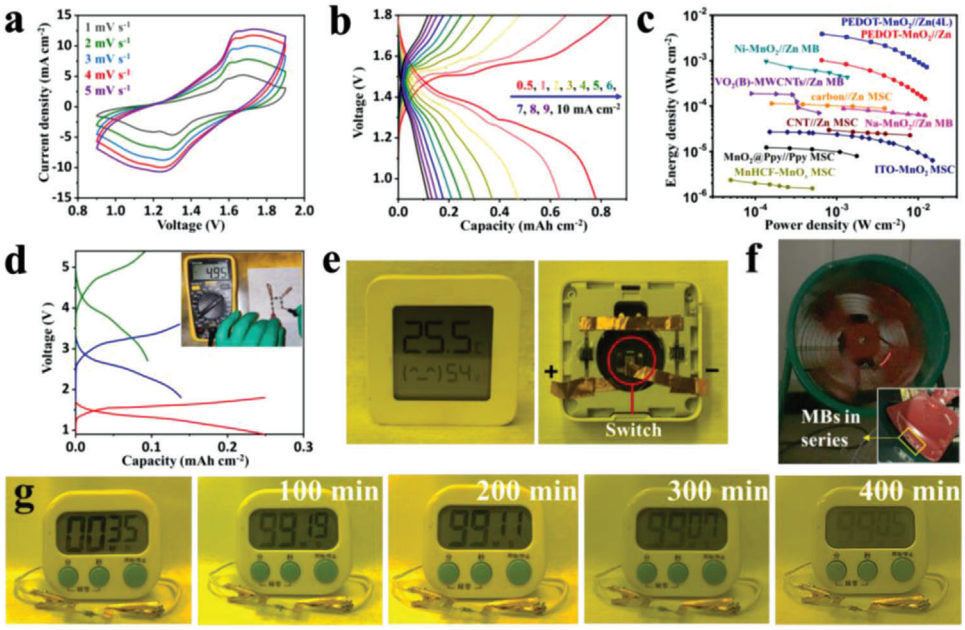

Figure 4. Electrochemical performance of PEDOT-MnO_2//Zn MB. a) The CV curves at different scan rates, b) the GCD curves at various current densities, and c) the Ragone plots based on the areal energy/power densities. d) Electrochemical performance of MBs in series. e) The digital hygro-thermometer is driven by MBs in series (without substrate). f) The LED-MBs system operates with high-speed rotation. g) Digital images show an electronic timer driving by a MB for ≈400 min.

high maximum volumetric density of 123 mWh cm^{-3} (denoted as PEDOT-MnO_2//Zn-m).

To investigate the potential application on microelectronic chips system, the series and integration performance of PEDOT-MnO_2//Zn MB was further demonstrated. The GCD curves at 5 mA cm^{-2} with the voltage windows of 1.8, 3.6, and 5.4 V for PEDOT-MnO_2//Zn MB, two PEDOT-MnO_2//Zn MBs in series, and three PEDOT-MnO_2//Zn MBs in series were exhibited in Figure 4d. The twofold and the threefold voltage window of MBs in series suggest good performance scalability. Compared to MESDs by "bottom–up" manufacture, the substrate-free microelectrodes for PEDOT-MnO_2//Zn MB show superior convenience in integration.[54] The term "substrate-free" denotes that the microelectrodes are processed without a substrate. When employed, the microelectrodes can be easily fastened to any surface. It is able to utilize the extra space and adopt scattered distribution into the microelectronic circuit with a "plug-in compatibility" embedding method (Figure S29, Supporting Information). The PEDOT-MnO_2//Zn MBs in series are able to applicate in a commercial digital hygro-thermometer and provide a stable voltage output of over 1 h. The substrate-free microelectrodes can be assembled on the devices' surface directly, and the thickness of the MB is reduced (Figure 4e; Movie S1, Supporting Information). Furthermore, the operando testing system for high-speed rotating parts (such as aircraft rotors) is hard to realize currently, and one of the essential reasons is difficulty to wire for micro sensors' power supply. A light-emitting diode (LED)-MBs system is integrated on the surface of an axial-flow fan with 1450 rpm rotation speed, 149 Pa full pressure, 5870 m^3 h^{-1} blowing rate, and high vibration, demonstrating the excellent operating stability of the MBs in the rotation facility (Figure 4f; Movie S2, Supporting Information). This system is expected to develop into a self-powered sensor system in the high-speed rotating component. To display the practical potential of PEDOT-MnO_2//Zn MB, an electronic timer is powered by the MB and stable operating for an ultra-long time of ≈400 min (Figure 4g).[55] To highlight the excellent standardization, integrability, and expansibility of the substrate-free microelectrodes, a MB with four layers stacked microelectrodes is fabricated (denoted as PEDOT-MnO_2//Zn(4L) MB). PEDOT-MnO_2//Zn(4L) MB delivers a fourfold areal capacity (2.94 mAh cm^{-2} at 0.5 mA cm^{-2}) than that of PEDOT-MnO_2//Zn MB without any rate capacity reduction. Remarkably, the ultrahigh areal energy density of PEDOT-MnO_2//Zn(4L) MB of 3.87 mWh cm^{-2} makes it among the best performance MBs (Figure S30 and Table S1, Supporting Information). These excellent features indicate that the PEDOT-MnO_2//Zn MB is a promising class of electronic components to satisfy certain practical application requirements and present on-chip integration technology.

3. Conclusion

In summary, we demonstrate a PEDOT-MnO_2//Zn MB by electrodeposited PEDOT-MnO_2 film on a 3D macroporous Ni frame interdigital microelectrode. The 3D frame with high thickness offers sufficient space and surface area for active materials and provides an abundant pathway for electron/ion transport. Benefiting from the 3D macroporous microelectrode with high mass-loading active material, the fabricated PEDOT-MnO_2//Zn MB exhibits an ultrahigh areal capacity of 0.78 mAh cm^{-2} (0.5 mA cm^{-2}), an excellent areal energy density of 1.02 mWh cm^{-2} (0.65 mW cm^{-2}), and a relatively high areal power density of 12.16 mW cm^{-2} (0.16 mWh cm^{-2}). The MB with high electrochemical performance is capable of operating in a high-speed rotating component stably and driving an electronic timer for

≈400 min. Benefiting from the substrate-free microelectrodes, the PEDOT-MnO_2//Zn(4L) MB shows outstanding integrability and expansibility and delivers ultrahigh areal capacity of 2.94 mAh cm^{-2} and energy density of 3.87 mWh cm^{-2}. In addition, the PEDOT-MnO_2//Zn MB shows excellent integration and high weldability, and is capable of embedding in microelectronic circuits facilely. Moreover, the commercial large-scale wet etching procedure for microelectrodes can significantly reduce the costs and vastly increase the effectiveness of research and manufacture. Owing to a combination of ultrahigh areal energy density, high power density, excellent integration, and outstanding industrialization prospects, PEDOT-MnO_2//Zn MB exhibits high potential in the next-generation self-powered microelectronic systems.

4. Experimental Section

Chemicals: Manganese acetate tetrahydrate ($Mn(CH_3COO)_2{\cdot}4H_2O$), manganese sulfate monohydrate ($MnSO_4{\cdot}H_2O$), zinc sulfate heptahydrate ($ZnSO_4{\cdot}7H_2O$), nickel sulfate hexahydrate ($NiSO_4{\cdot}6H_2O$), ammonium sulfate ($(NH_4)_2SO_4$), magnesium nitrate ($Mg(NO_3)_2{\cdot}9H_2O$), sodium sulfate anhydrous (Na_2SO_4), multi-walled carbon nanotube (MWCNT), 3,4-ethylenedioxythiophene (EDOT), and xanthan gum were the chemicals used. All the chemicals were used without further purification.

Fabrication of 3D Macroporous Ni Frame Microelectrode: 3D macroporous Ni frame microelectrode was fabricated through an electrodeposition process.[56] First, an electrolyte containing 0.75 M $(NH_4)_2SO_4$ and 0.1 M $NiSO_4$ was prepared. A Ni interdigital microelectrode, a Pt foil, and a saturated Ag/AgCl were employed as working electrode, counter electrode, and reference electrode, respectively. The typical electrodeposition was performed with a constant voltage of −4.5 V for 100 s. The 3D macroporous Ni frame microelectrode was rinsed with deionized (DI) water, followed by drying at 90 °C for 30 min.

Fabrication of PEDOT-MnO_2 Microelectrode: The PEDOT-MnO_2 microelectrodes were fabricated by a CV electrodeposition process in an electrolyte (20 mL) contained $(CH_3COO)_2Mn{\cdot}4H_2O$ (0.245 g) and EDOT (100 µL). The 3D macroporous Ni frame microelectrode, a Pt foil, and a saturated Ag/AgCl were employed as working electrode, counter electrode, and reference electrode, respectively. The electrodeposition process was performed with the potential window of 0–1.2 V at 50 mV s^{-1} for 10, 30, 50, 70, and 90 cycles. The achieved PEDOT-MnO_2 microelectrodes were rinsed with DI water and dried at 90 °C for 30 min.

Fabrication of Zn@CNTs Microelectrode: The Zn@CNTs microelectrode was fabricated by a two-step deposition process. First, an electrophoresis process with a brass interdigital microelectrode as the negative electrode and a Pt foil as the positive electrode in a dispersion liquid was employed, which contained 20 mL absolute alcohol, 20 mg carbon nanotubes, and 5 mg $Mg(NO_3)_2$. The electrophoresis procedure was worked at a constant voltage of 10 V for 3 min with a direct current stabilized power supply. After drying at 80 °C for 10 min, an interdigital microelectrode with CNT-coated fingers was achieved. Then, the Zn@CNTs microelectrode was achieved by an electrodeposition process in a solution of 0.5 M $NaSO_4$ and 0.5 M $ZnSO_4$ at −1.1 V for 600 s by a CHI760D. In this procedure, the CNT-coated microelectrode, a Pt foil, and a saturated Ag/AgCl electrode were employed as the working electrode, the counter electrode, and the reference electrode, respectively.

Preparation of the Electrolytes: The aqueous electrolyte was prepared by dissolving 2 M $ZnSO_4$ and 0.4 M $MnSO_4$ in 20 mL DI water. The gel-electrolyte was prepared by adding 0.7 g xanthan gum into the 20 mL above aqueous electrolyte, followed by mechanical stirring under 40 °C for an hour.

Assembly of PEDOT-MnO_2//Zn MB: The PEDOT-MnO_2//Zn MB was assembly by pasting PEDOT-MnO_2 cathode and Zn@CNTs anode microelectrodes on a PET film by cyanoacrylate glue under optical alignment. After solidification of cyanoacrylate glue, the gel-electrolyte was coated on the microelectrodes and packaged with a square PE film with edge sealing.

Materials and Devices Characterization: Scanning electron microscopy (SEM) images were obtained with a JEOL JSM-7100F SEM at an acceleration voltage of 20.0 kV. Energy dispersive X-ray spectroscopy (EDS) results were recorded by an Oxford IE250 system. X-ray photoelectron spectroscopy (XPS) results were recorded by the VG Multi Lab 2000. High-resolution transmission electron microscopy (HRTEM) and selected area electron diffraction (SAED) images were obtained with a Titan G2 60–300. X-ray diffraction (XRD) results were recorded by a D8 DISCOVER X-ray diffractometer with Cu Kα radiation (λ = 1.5418 Å).

Electrochemical Measurements: The CV and GCD results were recorded by a CHI760D to examine the electrochemical performances of PEDOT-MnO_2 microelectrodes and the PEDOT-MnO_2//Zn MBs. The CV and GCD tests of PEDOT-MnO_2 microelectrodes and PEDOT-MnO_2//Zn MBs were measured by a two-electrode system. The EIS results were measured in a frequency range of 0.01–300000 Hz by the CHI760D with a standard three-electrode system. GITT results were conducted on Land T2001A battery testing stations with a voltage window range of 0.9–1.8 V. The current pulse of 1 mA cm^{-2} for 5 min and the following relaxation for 30 min were applied in GITT test.

The areal capacity (C_h) of PEDOT-MnO_2 microelectrode was according to the following equation:[15]

$$C_h = \frac{I\Delta t}{A\Delta V} \tag{1}$$

where I, Δt, ΔV, and A were the discharge current, the discharge time after IR drop, the potential window, and the print area of half of the full device (0.07 cm^2, Figure S1a,b, Supporting Information), respectively.

The areal capacity (C_f) of PEDOT-MnO_2//Zn MB was according to the following equations:[15]

$$C_f = \frac{I\Delta t}{A\Delta V} \tag{2}$$

where I, Δt, ΔV, and A were the discharge current, the discharge time after IR drop, the voltage window, and the print area of the full device (0.14 cm^2, Figure S1a,b, Supporting Information), respectively.

The electrochemical kinetic analysis of microelectrodes was according to the following equations:[45]

$$i = av^b \tag{3}$$

$$\log(i) = \text{blog}(v) + \log(a) \tag{4}$$

where i was the current, v was the scan rate, and a and b were the fitted parameters.

The current $i(V)$ at a given potential V obeyed the relations of:

$$\text{i}(V) = k_1v + k_2v^{1/2} \tag{5}$$

Where $i(V)$, k_1v, and $k_2v^{1/2}$ are the measured current, current from the surface capacitive contribution, and current from the diffusion-controlled contribution, respectively.

The ions diffusion coefficients were measured by galvanostatic intermittent titration technique (GITT) and calculated based on the following equation:[45]

$$D_{GITT} = \frac{4}{\pi\Delta\tau}\left(\frac{m_BV_M}{M_BS}\right)\left(\frac{\Delta E_s}{\Delta E_\tau}\right)^2 \tag{6}$$

where m_B was the weight of the active materials, M_B referred to the molecular weight, V_m was the molar volume, S was the surface area of microelectrode, τ was the duration time of the current pulse, ΔE_s was the voltage

difference measured at the end of the relaxation period for two successive steps, and ΔE_τ was the difference between the initial voltage and final voltage during the discharge pulse time τ after eliminating the IR drop.

The areal energy density (E_a) and areal power density (P_a) were calculated using the following equation:[15]

$$E_a = \frac{\int_0^t IV(t)\,dt}{A} \tag{7}$$

$$P_a = \frac{E_a}{t} \times 3600 \tag{8}$$

where t referred to the discharge time, I was the discharge current, $V(t)$ was the discharge voltage at t, dt was the time differential, and A was the print area of the full device.

The volumetric energy density (E_v) and volumetric power density (P_v) were calculated using the following equation:[15]

$$E_v = \frac{\int_0^t IV(t)\,dt}{A} \tag{9}$$

$$P_v = \frac{E_v}{\Delta t} \times 3600 \tag{10}$$

where t referred to the discharge time, I was the discharge current, $V(t)$ was the discharge voltage at t, dt was the time differential, and A was the volume of the full device.

Supporting Information

Supporting Information is available from the Wiley Online Library or from the author.

Acknowledgements

This work was supported by the National Key Research and Development Program of China (Grant No. 2020YFA0715000), the National Natural Science Foundation of China (Grant Nos. 51832004, 52172233, 52272234, 52127816), the Key Research and Development Program of Hubei Province (Grant No. 2021BAA070), Foshan Xianhu Laboratory of the Advanced Energy Science and Technology Guangdong Laboratory (Grant Nos. XHT2020-005, XHT2020-003), Independent Innovation Project of the Hubei Longzhong Laboratory (2022ZZ-20), and Sanya Science and Education Innovation Park of Wuhan University of Technology (2021KF0011).

Conflict of Interest

The authors declare no conflict of interest.

Data Availability Statement

The data that support the findings of this study are available from the corresponding author upon reasonable request.

Keywords

3D macroporous frame microelectrodes, aqueous batteries, high integrability, Zn–Mn microbatteries

Received: February 23, 2023
Revised: April 18, 2023
Published online:

[1] M. Beidaghi, Y. Gogotsi, *Energy Environ. Sci.* **2014**, *7*, 867.
[2] N. A. Kyeremateng, T. Brousse, D. Pech, *Nat. Nanotechnol.* **2017**, *12*, 7.
[3] G. Wang, L. Zhang, J. Zhang, *Chem. Soc. Rev.* **2012**, *41*, 797.
[4] N. Choudhary, C. Li, J. Moore, N. Nagaiah, L. Zhai, Y. Jung, J. Thomas, *Adv. Mater.* **2017**, *29*, 1605336.
[5] Y. He, P. Zhang, M. Wang, F. Wang, D. Tan, Y. Li, X. Zhuang, F. Zhang, X. Feng, *Mater. Horiz.* **2019**, *6*, 1041.
[6] Z. Liu, Z.-S. Wu, S. Yang, R. Dong, X. Feng, K. Müllen, *Adv. Mater.* **2016**, *28*, 2217.
[7] W. Yang, L. He, X. Tian, M. Yan, H. Yuan, X. Liao, J. Meng, Z. Hao, L. Mai, *Small* **2017**, *13*, 1700639.
[8] X. Tian, M. Shi, X. Xu, M. Yan, L. Xu, A. Minhas-Khan, C. Han, L. He, L. Mai, *Adv. Mater.* **2015**, *27*, 7476.
[9] P. Sun, X. Li, J. Shao, P. V. Braun, *Adv. Mater.* **2020**, *33*, 2006229.
[10] C. Lethien, J. L.e Bideau, T. Brousse, *Energy Environ. Sci.* **2019**, *12*, 96.
[11] M. Beidaghi, C. Wang, *Electrochim. Acta* **2011**, *56*, 9508.
[12] Z.-S. Wu, K. Parvez, S. Li, S. Yang, Z. Liu, S. Liu, X. Feng, K. Müllen, *Adv. Mater.* **2015**, *27*, 4054.
[13] P. Huang, C. Lethien, S. Pinaud, K. Brousse, R. Laloo, V. Turq, M. Respaud, A. Demortière, B. Daffos, P. L. Taberna, B. Chaudret, Y. Gogotsi, P. Simon, *Science* **2016**, *351*, 691.
[14] W. Yang, Y. Zhu, Z. Jia, L. He, L. Xu, J. Meng, M. Tahir, Z. Zhou, X. Wang, L. Mai, *Adv. Energy Mater.* **2020**, *10*, 2001873.
[15] Z. Hao, L. Xu, Q. Liu, W. Yang, X. Liao, J. Meng, X. Hong, L. He, L. Mai, *Adv. Funct. Mater.* **2019**, *29*, 1808470.
[16] J. H. Pikul, H. Gang Zhang, J. Cho, P. V. Braun, W. P. King, *Nat. Commun.* **2013**, *4*, 1732.
[17] J. H. Pikul, J. Liu, P. V. Braun, W. P. King, *J. Power Sources* **2016**, *315*, 308.
[18] X. Xia, D. Chao, Z. Fan, C. Guan, X. Cao, H. Zhang, H. J. Fan, *Nano Lett.* **2014**, *14*, 1651.
[19] M. Wang, X. Zheng, X. Zhang, D. Chao, S. Z. Qiao, H. N. Alshareef, Y. Cui, W. Chen, *Adv. Energy Mater.* **2020**, *11*, 2002904.
[20] M. Li, Q. He, Z. Li, Q. Li, Y. Zhang, J. Meng, X. Liu, S. Li, B. Wu, L. Chen, Z. Liu, W. Luo, C. Han, L. Mai, *Adv. Energy Mater.* **2019**, *9*, 1901469.
[21] X. Shan, D. S. Charles, W. Xu, M. Feygenson, D. Su, X. Teng, *Adv. Funct. Mater.* **2017**, *28*, 1703266.
[22] S. Zhu, L. Li, J. Liu, H. Wang, T. Wang, Y. Zhang, L. Zhang, R. S. Ruoff, F. Dong, *ACS Nano* **2018**, *12*, 1033.
[23] B. Zhang, Y. Liu, X. Wu, Y. Yang, Z. Chang, Z. Wen, Y. Wu, *Chem. Commun.* **2014**, *50*, 1209.
[24] Z. Lv, Y. Luo, Y. Tang, J. Wei, Z. Zhu, X. Zhou, W. Li, Y. Zeng, W. Zhang, Y. Zhang, D. Qi, S. Pan, X. J. Loh, X. Chen, *Adv. Mater.* **2018**, *30*, 1704531.
[25] Y. Zhao, C. Chang, F. Teng, Y. Zhao, G. Chen, R. Shi, G. I. N. Waterhouse, W. Huang, T. Zhang, *Adv. Energy Mater.* **2017**, *7*, 1700005.
[26] M. Song, H. Tan, D. Chao, H. J. Fan, *Adv. Funct. Mater.* **2018**, *28*, 1802564.
[27] J. Liu, C. Guan, C. Zhou, Z. Fan, Q. Ke, G. Zhang, C. Liu, J. Wang, *Adv. Mater.* **2016**, *28*, 8732.
[28] J. Wang, J. Liu, M. Hu, J. Zeng, Y. Mu, Y. Guo, J. Yu, X. Ma, Y. Qiu, Y. Huang, *J. Mater. Chem. A* **2018**, *6*, 11113.
[29] L. Gao, Z. Li, Y. Zou, S. Yin, P. Peng, Y. Shao, X. Liang, *iScience* **2020**, *23*, 101348.
[30] Y. Zeng, X. Zhang, Y. Meng, M. Yu, J. Yi, Y. Wu, X. Lu, Y. Tong, *Adv. Mater.* **2017**, *29*, 1700274.
[31] L. Jiang, D. Dong, Y.-C. Lu, *Nano Res. Energy* **2022**, *1*, e9120003.
[32] B. He, Q. Zhang, L. Li, J. Sun, P. Man, Z. Zhou, Q. Li, J. Guo, L. Xie, C. Li, X. Wang, J. Zhao, T. Zhang, Y. Yao, *J. Mater. Chem. A* **2018**, *6*, 14594.

[33] M. Tahir, L. He, W. A. Haider, W. Yang, X. Hong, Y. Guo, X. Pan, H. Tang, Y. Li, L. Mai, *Nanoscale* **2019**, *11*, 7761.
[34] Z. Ye, T. Li, G. Ma, Y. Dong, X. Zhou, *Adv. Funct. Mater.* **2017**, *27*, 1704083.
[35] Y. Zhang, Z. Hu, Y. An, B. Guo, N. An, Y. Liang, H. Wu, *J. Power Sources* **2016**, *311*, 121.
[36] B. Anothumakkool, R. Soni, S. N. Bhange, S. Kurungot, *Energy Environ. Sci.* **2015**, *8*, 1339.
[37] J. F. Serrano-Claumarchirant, A. M. Igual-Muñoz, M. Culebras, M. N. Collins, A. Cantarero, C. M. Gómez, *Adv. Mater. Interfaces* **2021**, *8*, 2100951.
[38] X. Shen, X. Wang, Y. Zhou, Y. Shi, L. Zhao, H. Jin, J. Di, Q. Li, *Adv. Funct. Mater.* **2021**, *31*, 2101579.
[39] Q. Li, L. Li, P. Wu, N. Xu, L. Wang, M. Li, A. Dai, K. Amine, L. Mai, J. Lu, *Adv. Energy Mater.* **2019**, *9*, 1901153.
[40] J. Ji, J. Yao, Y. Xu, H. Wan, B. Zhang, L. Lv, J. Li, N. Wang, J. Zhang, G. Ma, L. Tao, H. Wang, Y. Wang, H. Wang, *Energy Environ. Mater.* **2023**, *6*, e12340.
[41] X. Guo, J. Zhou, C. Bai, X. Li, G. Fang, S. Liang, *Mater. Today Energy* **2020**, *16*, 100396.
[42] H. Liu, G. Zhang, L. Wang, X. Zhang, Z. Zhao, F. Chen, L. Song, H. Duan, *ACS Appl. Energy Mater.* **2021**, *4*, 10414.
[43] X. Chen, Z. Cao, L. Xing, Y. Liao, Y. Qiu, W. Li, *Nanoscale* **2017**, *9*, 18467.
[44] T. Brezesinski, J. Wang, S. Tolbert, B. Dunn, *Nat. Mater.* **2010**, *9*, 146.
[45] B. Wang, Y. Zeng, P. Chen, J. Hu, P. Gao, J. Xu, K. Guo, J. Liu, *ACS Appl. Mater. Interfaces* **2022**, *14*, 36079.
[46] P. Xu, H. Yi, G. Shi, Z. Xiong, Y. Hu, R. Wang, H. Zhang, B. Wang, *Dalton Trans.* **2022**, *51*, 4695.
[47] J. Shi, S. Wang, X. Chen, Z. Chen, X. Du, T. Ni, Q. Wang, L. Ruan, W. Zeng, Z. Huang, *Adv. Energy Mater.* **2019**, *9*, 1901957.
[48] P. Zhang, Y. Li, G. Wang, F. Wang, S. Yang, F. Zhu, X. Zhuang, O. G. Schmidt, X. Feng, *Adv. Mater.* **2018**, *31*, 1806005.
[49] Q. Zhang, J. Zhang, Z. Zhou, L. Wei, Y. Yao, *J. Mater. Chem. A* **2018**, *6*, 20145.
[50] G. Sun, H. Yang, G. Zhang, J. Gao, X. Jin, Y. Zhao, L. Jiang, L. Qu, *Energy Environ. Sci.* **2018**, *11*, 3367.
[51] J. Du, Y. Zhao, Z. Zhang, X. Mu, X. Jiang, B. Huang, Y. Zhang, S. Zhang, Z. Zhang, E. Xie, *J. Mater. Chem. A* **2019**, *7*, 6220.
[52] J. Gao, C. Shao, S. Shao, F. Wan, C. Gao, Y. Zhao, L. Jiang, L. Qu, *Small* **2018**, *14*, 1801809.
[53] J. Liang, B. Tian, S. Li, C. Jiang, W. Wu, *Adv. Energy Mater.* **2020**, *10*, 2000022.
[54] C. Gao, J. Huang, Y. Xiao, G. Zhang, C. Dai, Z. Li, Y. Zhao, L. Jiang, L. Qu, *Nat. Commun.* **2021**, *12*, 2647.
[55] X. Jin, L. Song, C. Dai, Y. Xiao, Y. Han, X. Li, Y. Wang, J. Zhang, Y. Zhao, Z. Zhang, N. Chen, L. Jiang, L. Qu, *Adv. Mater.* **2022**, *34*, 2109450.
[56] S. Sengupta, A. Patra, M. Akhtar, K. Das, S. B. Majumder, S. Das, *J. Alloys Compd.* **2017**, *705*, 290.